

USING ADAPTIVE MESH REFINEMENT TO SIMULATE TURBULENT WINGS AT HIGH REYNOLDS NUMBERS

Álvaro Tanarro

Linné FLOW Centre
KTH Mechanics
SE-100 44 Stockholm, Sweden
atdr@mech.kth.se

Fermín Mallor

Linné FLOW Centre
KTH Mechanics
SE-100 44 Stockholm, Sweden
mallor@kth.se

Nicolas Offermans

Linné FLOW Centre
KTH Mechanics
SE-100 44 Stockholm, Sweden
nof@mech.kth.se

Adam Peplinski

Linné FLOW Centre
KTH Mechanics
SE-100 44 Stockholm, Sweden
adam@mech.kth.se

Ricardo Vinuesa

Linné FLOW Centre
KTH Mechanics
SE-100 44 Stockholm, Sweden
rvinuesa@mech.kth.se

Philipp Schlatter

Linné FLOW Centre
KTH Mechanics
SE-100 44 Stockholm, Sweden
pschlatt@mech.kth.se

ABSTRACT

The implementation of adaptive mesh refinement (AMR) in Nek5000 is used for the first time on the simulation of the flow over wings. This is done by simulating the flow over a NACA4412 profile with 5° angle of attack at chord-based Reynolds number 200,000. The mesh is progressively refined by means of AMR which allows for high resolution near the wall whereas significantly larger elements are used in the far-field. The resultant mesh shows higher resolution than previous conformal meshes, and it allows for larger computational domains, which avoid the use of RANS to determine the boundary condition, all of this with, approximately, 3 times lower total number of grid points. The results of the turbulence statistics show a good agreement with the ones obtained with the conformal mesh. Finally, using AMR on wings leads to simulations at higher Reynolds numbers (*i.e.* $Re_c = 850,000$) in order to analyse the effect of adverse pressure gradients at high Reynolds numbers.

INTRODUCTION

Wall-bounded turbulence is of great relevance in a wide range of industrial applications such as turbine blades or aircraft wings among many others, since it is the main source of drag generation, which limits the performance of these devices. Drag reduction has become unavoidable in certain fields such as aircraft manufacturing due to the strong restrictions set on fuel consumption and pollution for the upcoming years. One region of improvement is the wings of the aircraft where a considerable amount of drag is generated in the turbulent boundary layers (TBLs) developing around them. These TBLs are very complex due to the streamwise pressure gradient (PG) caused by the airfoil curvature, which has a significant effect on the development of the boundary layer. The relevance of PG TBLs is supported by the numerous works related to its analysis, both experimental and numerical. Whereas the first studies of turbulent wings were conducted in wind tunnels (see for instance Coles & Wadcock, 1979; Wadcock, 1987), recent develop-

ments in the available computational power have allowed to perform accurate numerical simulations of cases equivalent to those carried out experimentally. Some examples of this are the large-eddy simulations (LESs) performed by Sato *et al.* (2016), Frère *et al.* (2018) and Vinuesa *et al.* (2018), where the flow around airfoils is simulated at Reynolds numbers based on inflow velocity and chord length (Re_c) of at least 1 million.

Numerical simulations are an excellent way to study fluid dynamics as they avoid typical wind-tunnel limitations such as the impact of the side walls on the flow, inaccuracies in the measurements or flow conditioning effects that might significantly affect the results. On the other hand, wind-tunnel experiments are an equally valuable option for high-Reynolds-numbers campaigns due to the extremely high cost of corresponding high-resolution numerical simulations. Despite the fact that it is currently possible to perform high-fidelity simulations at comparably high Re_c , we are still far from transportation aircraft, where $Re_c \sim O(10^7)$, which will only be accomplished through more efficient computational methods and improved computational power. In this project we keep increasing the achievable value of Re_c by using adaptive mesh refinement (AMR), which provides a better mesh flexibility and improves the current code performance at high Re_c , as discussed below. Here we compare the results obtained with a mesh constructed by means of AMR used to simulate the flow around a NACA4412 wing section with 5° angle of attack and $Re_c = 200,000$, with results of the same flow using a conformal mesh based on typical resolution requirements for turbulence simulations. Nevertheless, the ultimate aim of this project is to perform well-resolved LES of the turbulent boundary layers developing around a NACA4412 at $Re_c = 1,640,000$, *i.e.* the same Re_c as that of the experiment by Wadcock (1987), at various angles of attack up to around 12° . This will provide some insight on the effect of the angle of attack and allow to continue with the work of Vinuesa *et al.* (2018) to analyse the effect of adverse pressure gradients (APGs) at high Re_c .

SIMULATIONS WITH AMR

Solution-aware simulations methods such as adaptive mesh refinement (AMR) are a promising way to achieve high- Re simulations of complex cases with sufficient accuracy. The idea of this method is to automatically refine the mesh in the regions where higher resolution is needed, whereas the areas with less steep velocity gradients become coarsened. Although this idea is not new, its application to the spectral-element code Nek5000 (Fischer *et al.*, 2008) (which is employed in the present work) is very recent. Nek5000 has shown very high accuracy and efficiency for simulating turbulent flows with excellent parallel scalability (Offermans *et al.*, 2016). Nevertheless, one of the main limitations of Nek5000 when simulating complex geometries is the lack of mesh flexibility and thus the difficulty of creating suitably resolved boundary-layer meshes, since Nek5000 requires conforming hexahedral meshes (although it supports unstructured ones). Thus, the AMR implementation provides a significant performance improvement to the code. In addition, previous conformal meshes of the flow over wing sections presented two main issues: first, the conforming nature of the mesh causes an over-refinement of the far field, which considerably increases the number of grid points; and second, the large aspect ratio of the elements in the far field which increases the number of iterations required to solve the pressure, therefore decreasing significantly the code performance.

Description of the flow case

The flow under study consists of the turbulent boundary layers developing around a NACA4412 wing section at $Re_c = 200,000$ with an angle of attack of 5° . Here we consider a well-resolved LES, which will allow to accurately compute the largest scales of the flow while the smallest scales are modelled using a comparably simple relaxation filter (Schlatter *et al.*, 2004). The solution in each spectral-element is expanded using Lagrange interpolants of polynomial order $N = 7$. The flow over the airfoil is simulated in a rectangular domain with streamwise and vertical lengths $L_x = L_y = 40c$, as illustrated in Figure 1 (top), and spanwise length $L_z = 0.6c$. The airfoil is located at the centre of such domain and rotated in order to introduce the angle of attack of 5° . The boundary conditions are inflow with constant velocity $U_\infty = 1$ on the left, normal outflow condition with tangential $U_\infty = 1$ on top and bottom ends of the domain, stabilised outflow boundary condition on the right side of the domain and periodic boundary conditions in the spanwise direction.

Refinement method

We choose to adapt the mesh with the h -refinement method, which consists in splitting selected elements with an oct-tree (3D) or quad-tree (2D) structure. As a consequence, elements can share a fraction of an edge only and hanging nodes are allowed. The standard version of Nek5000 does not support such a feature and some modifications are required in the code.

Interpolation operators are introduced to ensure continuity at the interface between coarse and fine elements (Kruse, 1997). We verified in a previous work that the efficiency of the pressure solver is maintained despite the introduction of those operators (Peplinski *et al.*, 2018). Then, we rely on external libraries to keep track of the grid hierarchy and connectivity (p4est by Burstedde *et al.*, 2011) and for

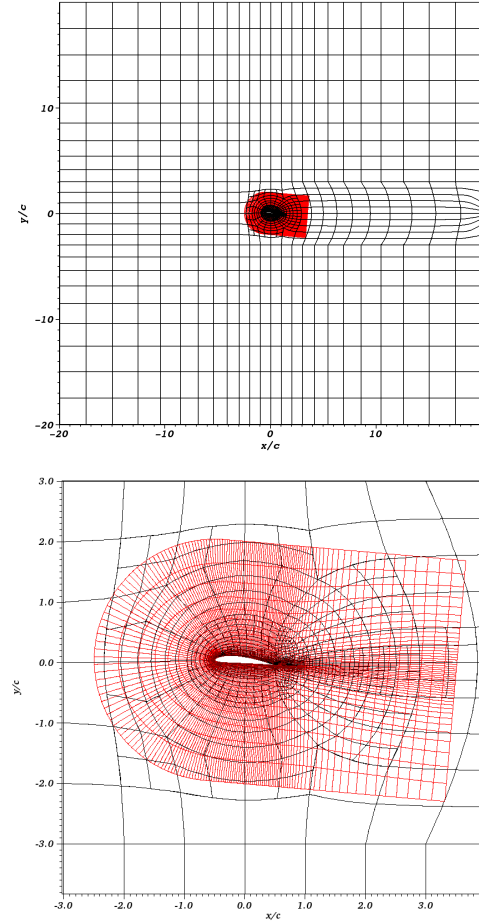


Figure 1: Comparison of computational domain using AMR for the simulation of a NACA4412 wing section at $Re_c = 200,000$ (marked in black) and the reference conformal mesh computational domain (marked in red). The upper plot shows zero-level AMR mesh before refinement and the lower plot shows the final AMR mesh.

grid partitioning (ParMETIS by Karypis & Kumar, 2009). The resulting grid management is done fully in parallel and a good scaling is maintained. One last change to the code is the modification of the preconditioner for the pressure equation. Nek5000 uses the combination of an overlapping Schwarz decomposition, resulting in small local problems, and a global coarse-grid solver. The local problems are modified to include the interpolation operator at refined interfaces. The coarse-grid problem must be adapted to exclude contributions from hanging nodes, which are not true degrees of freedom (Peplinski *et al.*, 2018).

Spectral error indicators

To estimate the error, we use the a posteriori error indicators developed by Mavriplis (1990). They provide an estimate of the L^2 -norm between the spectral-element solution at polynomial order N , *i.e.* u_N , and the exact solution u . Considering a 1D configuration for illustration, we can expand a solution $u(x)$ on a reference element in terms of the Legendre polynomials and express the associated spectral

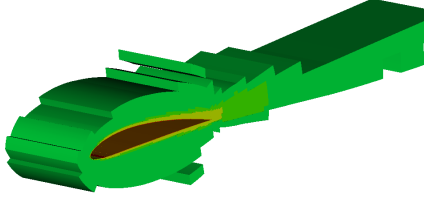


Figure 2: Regions of the domain covered by refinement levels higher than or equal to four for the final AMR mesh. The colours indicate the refinement level of the elements going from green (refinement level 4) to red (refinement level 7).

coefficients \hat{u}_k as

$$u(x) = \sum_{k=0}^{\infty} \hat{u}_k L_k(x) \quad \text{and} \quad \hat{u}_k = \frac{1}{\gamma_k} \int_{-1}^1 u(x) L_k(x) dx, \quad (1)$$

where L_k is the Legendre polynomial of order k and $\gamma_k = \|L_k\|_{L^2}^2$. The error on $\|u - u_N\|_{L^2}$ is attributed to two contributions: a truncation error due to the finite number of coefficients in the spectral expansion and a quadrature error. The estimated error indicator $\varepsilon \approx \|u - u_N\|_{L^2}$ is given by

$$\varepsilon = \left(\int_N^{\infty} \frac{\hat{u}(k)^2}{2} dk + \frac{\hat{u}_N^2}{2} \right)^{\frac{1}{2}}, \quad (2)$$

where it is assumed that the decay of the spectral coefficients follows the relation $\hat{u}_k \sim \hat{u}(k) = c \exp(-\sigma k)$. The parameters c and σ are obtained via a least-square best fit on the last four spectral coefficients. The computations are readily extended to the 2D and 3D cases. The main advantage of these estimators is their low computational cost, which is negligible in comparison to the time spent in the solver. From these indicators, we obtain an elementwise measure of the error at each timestep. The error is then averaged in time and mesh adaptation is performed periodically, at a given frequency. The criterion for refinement or coarsening is based on appropriate tolerances.

Design of the non-conformal mesh

The main objective with AMR is to use the tools for mesh refinement and error estimators to design an optimal mesh, where the error on the solution is as low and uniform as possible at a reasonable computational cost. Starting from the initial mesh, illustrated in Figure 1 (top) before any refinement based on error indicators is carried out, a minimum refinement level of 5 is imposed along the walls of the airfoil to ensure that the initial run is sufficiently resolved and stable. Then the simulation proceeds and error indicators are collected in time. At a fixed time interval, selected elements are refined based on the value of these indicators. The process is repeated until the refinement at the wall reaches the well-resolved LES resolution described by Vinuesa *et al.* (2018). For the present simulation, the resulting maximum level of refinement along the wall is 7. Once

the refinement process is over, the mesh remains fixed and the production runs are carried out. Let us note that this is a deliberate choice and not a limitation of our tools for AMR, which support dynamic mesh adaptation in the course of the simulation.

The resulting final mesh is shown in Figure 1 (bottom), along with an illustration of the conformal mesh used in previous works. Note that AMR enables the use of a significantly larger computational domain, where boundary conditions do not have to be extracted from a precursor Reynolds-averaged Navier–Stokes (RANS) simulation (Vinuesa *et al.*, 2017, 2018) and where the far-field elements are not over-refined. At the same time a high resolution is imposed near the wall and where needed in the wake. Figure 2 illustrates the different refinement levels for the final mesh at $Re_c = 200,000$, in which the elements with the highest refinement levels are located close to the wall or in certain regions of the wake due to the large gradients present in those regions. A validation of the results for the conformal and non-conformal meshes is performed in terms of the LES of the NACA4412 at $Re_c = 200,000$ and it is discussed below.

RESULTS

In this study we present the first wing simulations using AMR in Nek5000, therefore the first step in this work is to compare the results of AMR with simulations using a conformal mesh. The conformal case is similar to the one reported by Vinuesa *et al.* (2018) at $Re_c = 200,000$, with a slightly optimized mesh distribution. The main differences between the AMR and the conformal cases, in addition to the employed spectral-element mesh, are the polynomial order ($N = 7$ in this work and $N = 11$ in the conformal case), the tripping function (which was slightly modified in the AMR version by removing the forcing in regions far from the smoothing length) and the resulting resolution. Regarding the resolution normal to the wall, the grid spacing of the first point is the same as in the conformal case, *i.e.* $\Delta y_w^+ = 0.64$, where the superscript + denotes inner scaling. Note that inner scaling is obtained through the friction velocity $u_\tau = \sqrt{\tau_w/\rho}$ (where τ_w is the wall-shear stress and ρ the fluid density) and the viscous length $\ell^* = \nu/u_\tau$ (with ν being the kinematic viscosity). On the other hand, and due to the low-aspect-ratio elements of the non-conformal mesh, the spanwise and tangential resolutions of the AMR case are higher than the conformal mesh. In particular, in the conformal mesh $\Delta x_{\text{mean}}^+ = 18$ and $\Delta z_{\text{mean}}^+ = 9$, whereas in the non-conformal mesh $\Delta x_{\text{max}}^+ = 14$ and $\Delta z_{\text{max}}^+ = 7$ (note that the subscript ‘mean’ refers to the average grid spacing within a spectral element, and it constitutes a less strict resolution condition than the one given by the maximum grid spacing).

Even if the resolution of the non-conformal mesh around the wing is better than that of the conformal mesh, the total number of grid points in the mesh is also lower. The non-conformal mesh has a total of 234 million grid points (with a spanwise length of $L_z/c = 0.6$) whereas the conformal mesh, with $L_z/c = 0.2$, has a total of around 211 million grid points. This implies that the resolution of the conformal case, extended to the full width of $L_z/c = 0.6$, would require 634 million grid points (a number almost 3 times larger than the one of the AMR mesh). Therefore, the use of AMR in Nek5000 provides numerous advantages in comparison to the conformal mesh for the same wall-normal resolution: lower number of grid points, over 60

times larger computational domain (and, in turn, no need for the RANS-extracted boundary condition) and low-aspect-ratio elements.

The analysis of the AMR results is performed by computing several integral quantities and turbulence statistics of the TBLs around the wing, and comparing them with those obtained from the simulation using the conformal mesh. Regarding the turbulence statistics, these are averaged in the spanwise direction due to the homogeneity of the flow in this direction, and also in time over 6 flow-over times (note that the flow-over time is defined in terms of the inflow velocity and the chord length). All the turbulence statistics are expressed in terms of the local tangential (t) and normal directions (n), and the corresponding tensors are rotated as discussed by Vinuesa *et al.* (2017). In order to quantify the convergence of the results, the temporal averaging is expressed in terms of the normalised eddy-turnover time $ETT^* = tu_\tau/\delta_{99}L_z/L_{z,ref}$ as proposed by Vinuesa *et al.* (2016b), where t is the flow-over time and δ_{99} is the 99% boundary-layer thickness obtained with the method by Vinuesa *et al.* (2016a). This definition of the eddy-turnover time normalises the length of the homogeneous direction (in this case L_z) with respect to a reference length $L_{z,ref} = 3\delta_{99}$ defined by Flores & Jiménez (2010) as the minimum box size required to fully capture the largest structures in the logarithmic region. In terms of convergence as a function of the eddy-turnover time, the results from the high- Re DNS performed by Sillero *et al.* (2014) show that statistical convergence can be achieved by averaging for, approximately, 12 eddy-turnover times, whereas in this case the total averaging time is 50 eddy-turnover times at $x_{ss}/c = 0.8$. In the following, the subscripts ss and ps are employed to denote suction and pressure sides of the wing, respectively.

The first quantity under comparison is the Clauser pressure-gradient parameter $\beta = \delta^*/\tau_w dP_e/dx_t$, which represents the magnitude of the APG along the chord. The variables that define the Clauser pressure-gradient parameter are: δ^* which is the displacement thickness, P_e is the pressure at the boundary-layer edge and x_t is the distance from the leading edge measured along the direction tangential to the wing surface. Figure 3 shows β for both cases and, although there are small differences mainly at the beginning of the TBL and as it approaches the trailing edge, it can be stated that the results show a very good agreement. Note that in this case the inflection point at the location of maximum camber (*i.e.* $x_{ss}/c = 0.4$) observed at higher Reynolds numbers (Vinuesa *et al.*, 2018) is only visible in the AMR case, which has higher resolution close to the wing.

Next, the skin-friction coefficient normalised with the local edge velocity U_e , *i.e.* $C_f = 2(u_\tau/U_e)^2$, is shown in Figure 4. Our results show that C_f is slightly larger in the simulation with AMR than in the conformal case on both sides of the wing, a discrepancy that could possibly be attributed to the higher near-wall resolution of the former, although this will be investigated in further detail. The rapidly decreasing skin friction towards the trailing edge on the suction side, due to the progressively stronger APG, is very well reproduced in both simulations. The difference in the skin-friction coefficient leads to a similar discrepancy in the friction Reynolds number $Re_\tau = \delta_{99}u_\tau/\nu$, as can be observed in Figure 5. Furthermore, this figure reveals some differences between both simulations in the range $x/c \simeq 0.2 - 0.3$, which are due to the tripping of both simulations. Note the differences in the Re_τ curves beyond

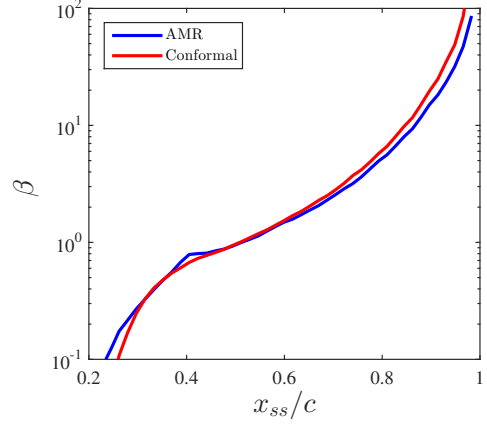


Figure 3: Clauser pressure-gradient parameter β on the suction side as a function of the distance from the leading edge, $Re_c = 200,000$.

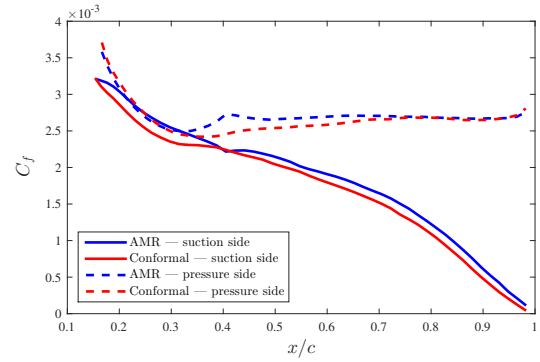


Figure 4: Streamwise evolution of the skin-friction coefficient C_f as a function of the distance from the leading edge.

this point are mainly due to the friction velocity u_τ , since the streamwise evolution of the boundary-layer thickness is in very good agreement in both simulations. This can be further observed in Figure 6, which shows the streamwise evolution of the Reynolds number based on momentum thickness $Re_\theta = U_e\theta/\nu$ in both cases. This figure shows the excellent agreement of both wing simulations on the suction and pressure sides.

Regarding turbulence statistics, mean tangential velocity and non-zero Reynolds stresses are presented at $x/c = 0.4$ and $x/c = 0.6$ in inner scaling. Starting with the inner-scaled tangential mean velocity profiles shown in Figure 7, the profile on the suction side at $x/c = 0.4$ shows a very good agreement between both cases. Nevertheless, the pressure side shows a small discrepancy in the mean velocity, which is a direct consequence of the difference in predicted wall-shear stress. Figure 4 shows smaller differences in C_f at $x/c = 0.6$, which result in a better agreement of the inner-scaled mean velocity profile on the pressure side. Furthermore, the mean velocity profile at $x_{ss}/c = 0.6$ is in reasonably good agreement in both simulations, given the small differences in wall-shear stress. This is a remarkable result, given the strong local pressure gradient at this location and the general complexity of the flow case.

Figure 8 shows the inner-scaled Reynolds stresses of

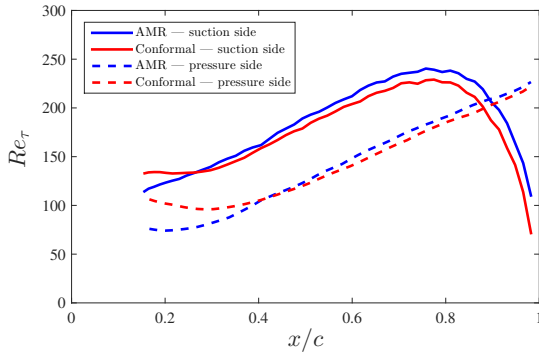


Figure 5: Streamwise evolution of the friction Reynolds number Re_τ .

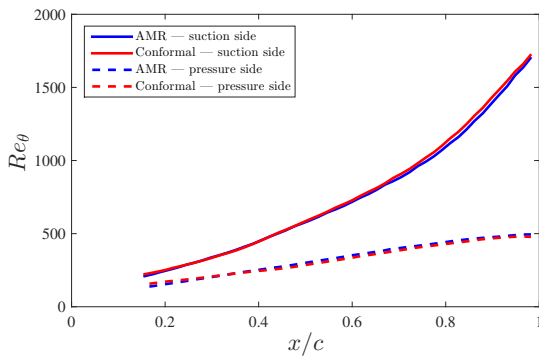


Figure 6: Streamwise evolution of the momentum-thickness Reynolds number Re_θ .

both cases on the suction side. The results at $x_{ss}/c = 0.4$ exhibit an excellent agreement in all the stresses, except for a slightly larger value of the near-wall peak of $\overline{u_t^2}^+$ predicted by the AMR simulation. This is also connected to the higher resolution in the spanwise direction in the AMR case. The Reynolds stresses are also in reasonably good agreement at $x_{ss}/c = 0.6$, in particular when it comes to the accumulation of energy in the outer region as a consequence of the streamwise APG. Note however the small deviations in the spanwise velocity fluctuations in the outer region.

CONCLUSIONS and OUTLOOK

In this study we have shown that, through the use of adaptive mesh refinement, it is possible to obtain high-quality meshes to simulate the turbulent boundary layers around wing sections using well-resolved LES. We have compared turbulence statistics at $Re_c = 200,000$ for a conformal case and an AMR-based configuration, which allows to reduce the required number of grid points by approximately a factor of 3. The agreement between both simulations is good in all the quantities, and the small observed discrepancy in the predicted skin-friction coefficient is connected to resolution differences. In Figure 9 we show an instantaneous visualization of the coherent vortical structures on a NACA4412 wing section, also with 5° angle of attack, at $Re_c = 850,000$. This on-going simulation is also obtained with AMR, and requires a total of 3.3 million spectral elements with $N = 8$, *i.e.* a total of 2.4 billion grid points. Note

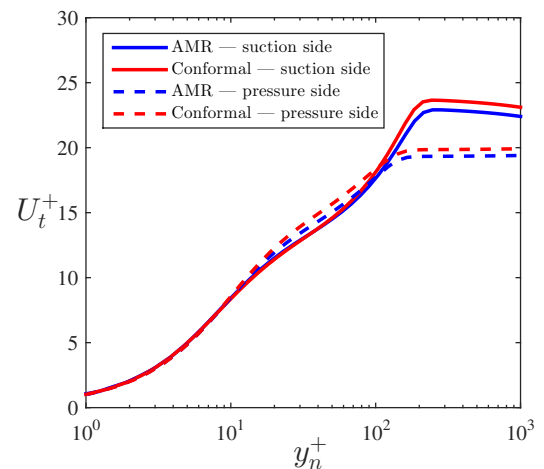
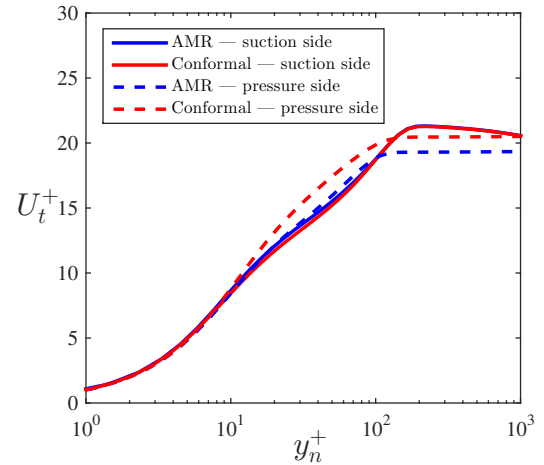


Figure 7: Inner-scaled tangential mean velocity profiles at (top) $x/c = 0.4$ and (bottom) $x/c = 0.6$.

the high level of detail of the turbulent structures around the wing obtained in this simulation. Ongoing work is aiming at reproducing the higher Reynolds number $Re_c = 1,640,000$ put forward by the experiment by Wadcock (1987). The same base mesh, with additional refinements, will be used for that case.

ACKNOWLEDGEMENTS

The simulations were performed on resources provided by the Swedish National Infrastructure for Computing (SNIC) at PDC. This research is funded by the Knut and Alice Wallenberg Foundation and is partially supported by the ExaFLOW H2020 Project (Project Number 671571).

REFERENCES

- Burstedde, C., Wilcox, L. C. & Ghattas, O. 2011 *p4est*: Scalable algorithms for parallel adaptive mesh refinement on forests of octrees. *SIAM J. Sci. Comput.* **33** (3), 1103–1133.
- Coles, D. & Wadcock, A. J. 1979 Flying-hot-wire study of flow past an NACA 4412 airfoil at maximum lift. *AIAA J.* **17** (4), 321–329.

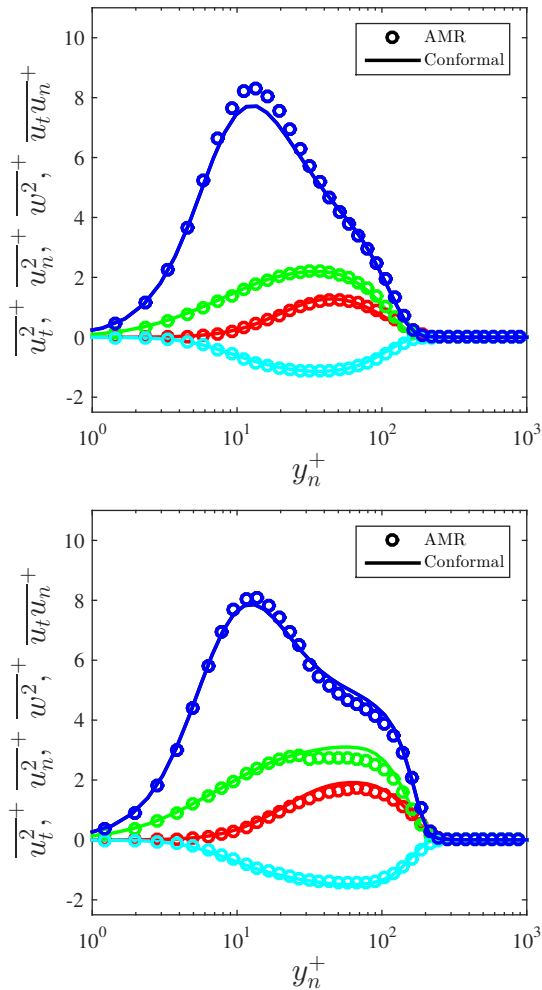


Figure 8: Inner-scaled non-zero Reynolds stresses corresponding to (top) $x_{ss}/c = 0.4$ and (bottom) $x_{ss}/c = 0.6$. The colors indicate: tangential (—), wall-normal (—), spanwise (—) velocity fluctuations and Reynolds-shear stress (—).

Fischer, P., Kruse, J., Mullen, J., Tufo, H., Lottes, J. & Kerkemeier, S. 2008 Nek5000: Open source spectral element CFD solver. Available at: <https://nek5000.mcs.anl.gov/>.

Flores, O. & Jiménez, J. 2010 Hierarchy of minimal flow units in the logarithmic layer. *Phys. Fluids* **22** (7), 071704.

Frère, A., Hillewaert, K., Chatelain, P. & Winckelmans, G. 2018 High Reynolds number airfoil: from wall-resolved to wall-modeled LES. *Flow Turbul. Combust.* **101**, 457–476.

Karypis, G. & Kumar, V. 2009 MeTis: Unstructured Graph Partitioning and Sparse Matrix Ordering System, Version 4.0. <http://www.cs.umn.edu/~metis>.

Kruse, G. W. 1997 Parallel nonconforming spectral element solution of the incompressible navier–stokes equations in three dimensions. PhD thesis, Brown University.

Mavriplis, C. 1990 A posteriori error estimators for adaptive spectral element techniques. In *Notes on Numerical Fluid Mechanics* (ed. P. Wesseling), pp. 333–342.

Offermans, N., Marin, O., Schanen, M., Gong, J., Fischer, P., Schlatter, P., Obabko, A., Peplinski, A., Hutchinson, M. & Merzari, E. 2016 On the strong scaling of the spec-

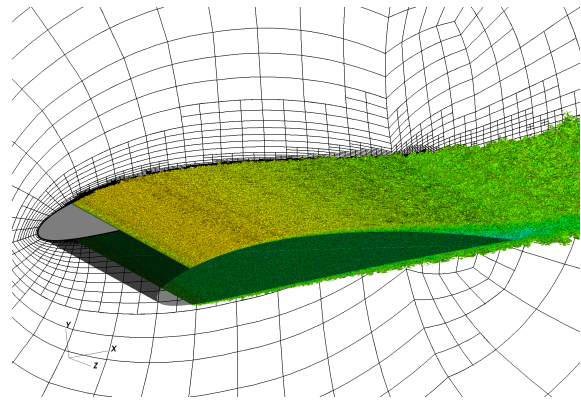


Figure 9: Instantaneous visualization of the flow around a NACA4412 wing section at $Re_c = 850,000$, showing coherent vortical structures identified with the λ_2 criterion. The spectral-element mesh is also shown (although not the individual grid points within elements), illustrating the various required refinement levels. The color indicates streamwise velocity, where blue and red denote low- and high-velocity regions, respectively.

tral element solver Nek5000 on petascale systems. In *Proceedings of the Exascale Applications and Software Conference 2016*, p. 5. ACM.

Peplinski, A., Offermans, N., Fischer, P. F. & Schlatter, P. 2018 Non-conforming elements in Nek5000: Pressure preconditioning and parallel performance. In *Proceedings of the International Conference On Spectral And High Order Methods, ICOSAHOM '18*. London, UK, to appear.

Sato, M., Asada, K., Nonomura, T., Kawai, S. & Fujii, K. 2016 Large-eddy simulation of NACA 0015 airfoil flow at Reynolds number of 1.6×10^6 . *AIAA J.* **55** (2), 673–679.

Schlatter, P., Stolz, S. & Kleiser, L. 2004 LES of transitional flows using the approximate deconvolution model. *Int. J. Heat Fluid Flow* **25** (3), 549–558.

Sillero, J. A., Jiménez, J. & Moser, R. D. 2014 Two-point statistics for turbulent boundary layers and channels at Reynolds numbers up to $\delta^+ \simeq 2000$. *Phys. Fluids* **26** (10), 105109.

Vinuesa, R., Bobke, A., Örlü, R. & Schlatter, P. 2016a On determining characteristic length scales in pressure-gradient turbulent boundary layers. *Phys. Fluids* **28**, 055101.

Vinuesa, R., Hosseini, S. M., Hanifi, A., Henningson, D. S. & Schlatter, P. 2017 Pressure-gradient turbulent boundary layers developing around a wing section. *Flow Turbul. Combust.* **99**, 613–641.

Vinuesa, R., Negi, P. S., Atzori, M., Hanifi, A., Henningson, D. S. & Schlatter, P. 2018 Turbulent boundary layers around wing sections up to $Re_c = 1,000,000$. *Int. J. Heat Fluid Flow* **72**, 86–99.

Vinuesa, R., Prus, C., Schlatter, P. & Nagib, H. M. 2016b Convergence of numerical simulations of turbulent wall-bounded flows and mean cross-flow structure of rectangular ducts. *Meccanica* **51** (12), 3025–3042.

Wadcock, A. J. 1987 Investigation of low-speed turbulent separated flow around airfoils. *NASA Tech. Rep. (NASA-CF-177450)*.